Supplemental Information

Mechanism of Cytokinetic Contractile Ring Constriction in Fission Yeast

Matthew R. Stachowiak, Caroline Laplante, Harvey F. Chin, Boris Guirao, Erdem Karatekin, Thomas D. Pollard and Ben O'Shaughnessy

SUPPLEMENTAL FIGURES

- Figure S1, related to Figure 1. Cell polarity, node motions, and myosin concentration in contractile rings.
- Figure S2, related to Figure 2. Bidirectional motions of formin and myosin in contractile rings, spatial distribution of formin in rings, and measurement of the protoplast membrane tension by aspiration.
- Figure S3, related to Figure 3. Contractile ring thickness, testing the turnover mechanisms assumed in the simulation, and correlation function of formin in the ring.
- Figure S4, related to Figure 6. Comparison of observed and model-predicted ring shapes and length evolutions during ring constriction in fission yeast protoplasts.

SUPPLEMENTAL TABLES

- Table S1, related to Figure 3. Key parameter values of the ring simulation.
- Table S2, related to Experimental Procedures. *S. pombe* strains used in this study

SUPPLEMENTAL MOVIES

- Movie S1, related to Figure 1. Diffusion of nodes marked with Rlc1p-3GFP in a protoplast.
- Movie S2, related to Figure 1. Directed, stop-go motions of nodes marked with Rlc1p-3GFP in a protoplast.
- Movie S3, related to Figure 1. Sliding and constriction of a contractile ring marked with Rlc1p-3GFP in a compressed protoplast.
- Movie S4, related to Figure 2. Motions of formin Cdc12p-3YFP in the contractile ring of a compressed protoplast.
- Movie S5, related to Figure 2. Motions myosin-II marked with Rlc1p-tdTomato in the contractile ring of a compressed protoplast.
- Movie S6, related to Figure 4. Ring simulation under standard, "wild type" conditions.
- Movie S7, related to Figure 6. Comparison of observed and predicted ring constriction in a compressed protoplast with dimensions $h = 1.60$ μm and $R = 1.96$ μm.

EXTENDED EXPERIMENTAL PROCEDURES

- Measurement of ring tension.
- Simulation of the fission yeast contractile ring.
- Quantitative characterization of the ring organization: the sarcomericity, the bundling coefficient, and their relation to ring tension

- Sliding-constriction model of rings in protoplasts, and comparison to observed ring shapes and constriction rates.

SUPPLEMENTAL REFERENCES

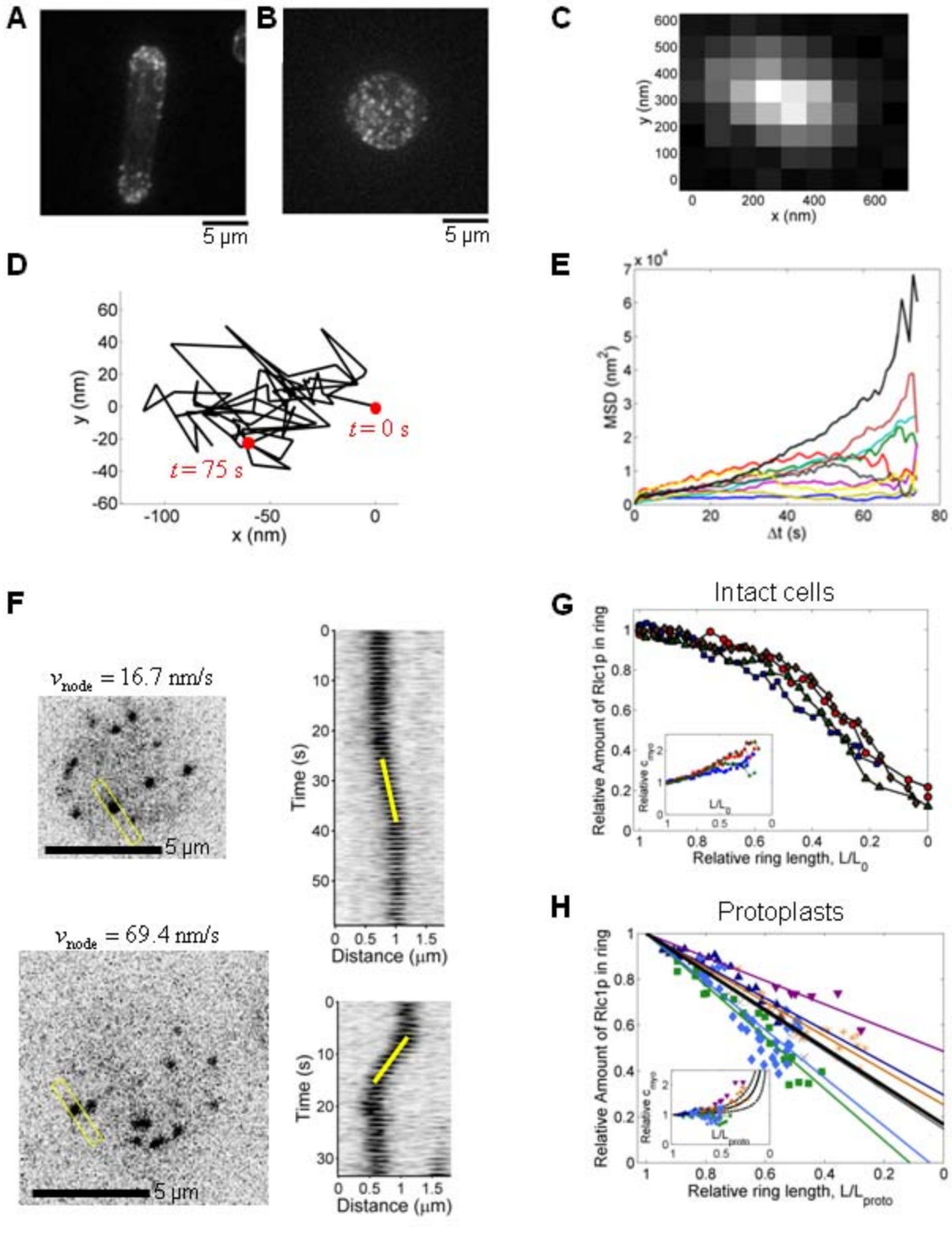
A
B
5 μm
5 μm
C
y (nm)
x (nm)
D
y (nm)
x (nm)
t = 0 s
t = 75 s
E
x 10^4
MSD (nm^2)
Δt (s)
F
v_node = 16.7 nm/s
5 μm
v_node = 69.4 nm/s
5 μm
Time (s)
Distance (μm)
Time (s)
Distance (μm)
G
Intact cells
Relative Amount of Rlc1p in ring
Relative ring length, L/L0
H
Protoplasts
Relative Amount of Rlc1p in ring
Relative ring length, L/Lproto

Figure S1

Figure S1, related to Figure 1. Cell polarity, node motions, and myosin concentration in contractile rings.

(A and B) Fluorescence micrographs of interphase cells expressing the calponin homology domain of Rng2p fused to GFP (GFP-CHD) (Martin and Chang, 2006) to highlight actin filaments concentrated in endocytic actin patches.

(A) Actin patches are located at the poles of intact cells, a hallmark of polarized growth (Drubin et al., 1988).

(B) In protoplasts, actin patches were distributed throughout the entire cortex, consistent with a loss of cell polarity.

(C) Fluorescence confocal image of Rlc1p-3GFP intensity of a diffusing node in a protoplast. Node position was determined from a best-fit 2D Gaussian.

(D) Trajectory at 1 s intervals of a single protoplast node undergoing diffusion.

(E) Mean square displacements (MSDs) of 10 individual protoplast nodes. A Bayesian analysis (Monnier et al., 2012) implicated free diffusion with 0.99 probability, while anomalous diffusion, confined diffusion, confinement, and directed flow each had probabilities <0.01.

(F) Reverse-contrast, confocal fluorescence microscopy images (Left) and kymographs (Right) of nodes in two protoplasts undergoing short bursts of directed, stop-go motions. Node velocities were determined by the slope of lines (yellow) drawn along node trajectories in kymographs.

(G and H) Time course of the fluorescence of Rlc1p-3GFP in constricting contractile rings. To measure the amount and concentration of myosin in contractile rings, sum projections were taken of stacks of confocal images (0.336 μm spacing) of cells expressing Rlc1p-3GFP. Ring intensity was measured as the fluorescence intensity in a polygon drawn around the ring minus the diffuse cytoplasmic background measured in a nearby region in the cell. These measurements were corrected for photobleaching using a curve of the fluorescence of the entire cell over time. Each symbol denotes a different cell.

(G) Myosin-II in contractile rings of 4 intact cells. Total amount of Rlc1p-3GFP fluorescence relative to initial value versus relative ring length. Inset: relative myosin-II concentration (fluorescence per ring length).

(H) Myosin-II in contractile rings of 6 protoplasts. Total amount of Rlc1p-3GFP fluorescence versus relative ring length. Myosin-II amount is relative to value at $L = L_{proto}$ assuming a linear relation. Thin solid lines: best-fit linear relations. Thick black line: mean of best-fit lines. Inset: relative concentration, showing mean (solid line) ± SEM (dashed lines).

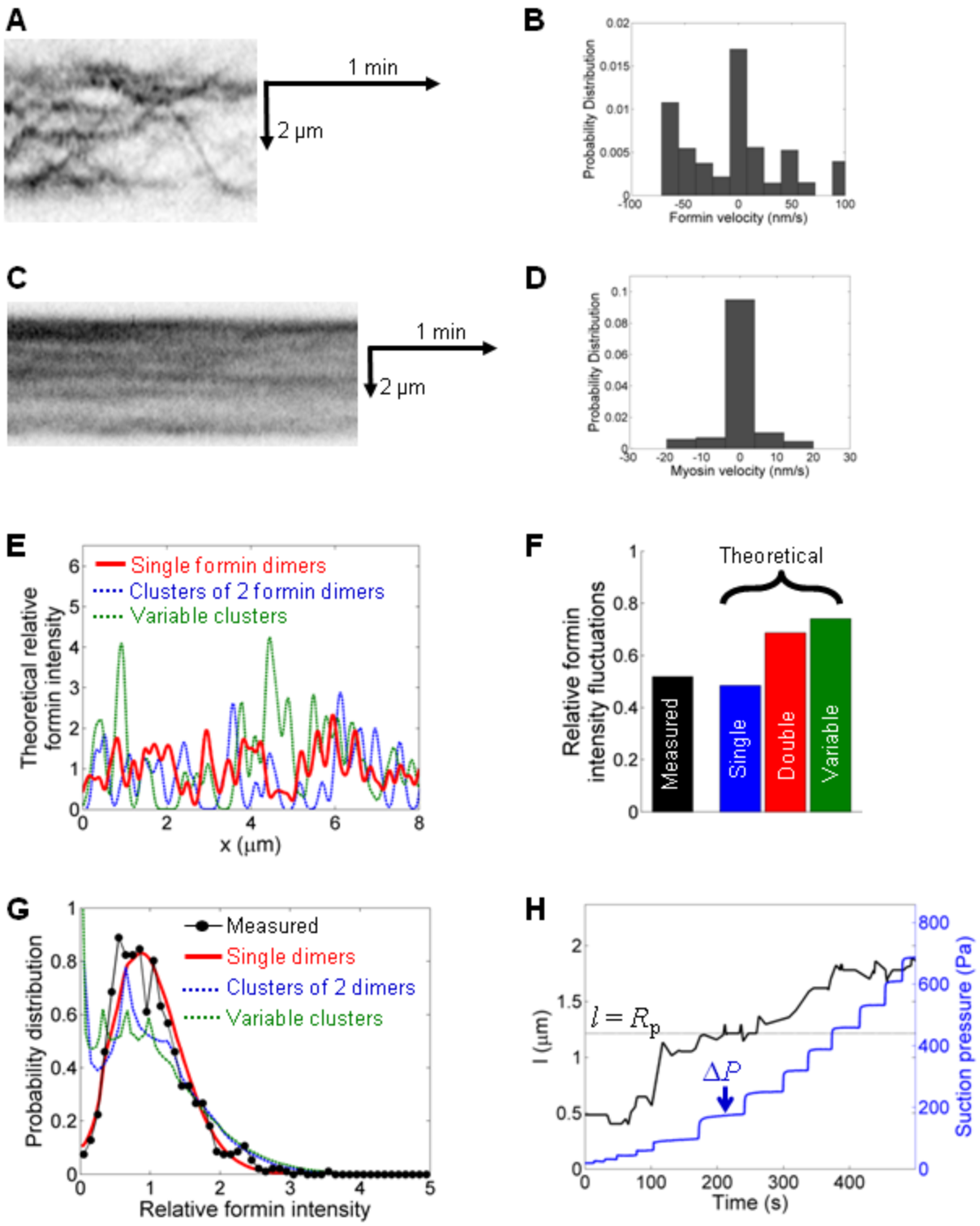
A
1 min
2 μm
B
Probability Distribution
Formin velocity (nm/s)
C
1 min
2 μm
D
Probability Distribution
Myosin velocity (nm/s)
E
Single formin dimers
Clusters of 2 formin dimers
Variable clusters
Theoretical relative formin intensity
x (μm)
F
Theoretical
Relative formin intensity fluctuations
Measured
Single
Double
Variable
G
Measured
Single dimers
Clusters of 2 dimers
Variable clusters
Probability distribution
Relative formin intensity
H
$l = R_p$
ΔP
l (μm)
Suction pressure (Pa)
Time (s)

Figure S2

Figure S2, related to Figure 2. Bidirectional motions of formin and myosin in contractile rings, spatial distribution of formin in rings, and measurement of the protoplast membrane tension by aspiration.

(A and C) Kymographs constructed from reverse-contrast fluorescence micrographs of cells expressing (A) fluorescent formin (Cdc12p-3YFP) or (C) fluorescent myosin-II (Rlc1p-tdTomato), showing motion of these proteins in contractile rings in compressed protoplasts. These results are from different cells to those analyzed in Fig. 2D-G.

(B and D) Velocity distributions of (B) formin and (D) myosin-II in the contractile rings depicted in (A) and (C). Both move bidirectionally along the ring.

(E) Examples of theoretical formin intensity profiles around the ring for three cases of formin clustering: single formin dimers, clusters of two dimers, and clusters of variable size containing 1, 2, and 3 dimers with equal probability. In each case the overall density was 15 dimers/μm of ring circumference, as previously measured in intact cells (Wu and Pollard, 2005). We assumed the same formin density in longer protoplast rings because a previous study showed that myosin-II density is the same in rings of different initial lengths (Mishra et al., 2012). Clusters were distributed randomly along the ring in accord with Fig. 2H-J. Intensity profiles were generated by convolving with an estimated point spread function (PSF) for YFP, a Gaussian with standard deviation 80 nm. Mean intensity is defined as 1.

(F) Formin intensity fluctuations (standard deviation divided by the mean) measured in protoplasts (n = 17 ring segments of mean length 4.5 μm), compared to the three theoretical formin distributions (calculated from 5,000 model rings of length 10 μm). The case of single formin dimers best matches the experimental data.

(G) Comparison of the probability distribution of formin intensity values measured in protoplasts (n = 17 rings) to the probability distribution of intensities for the three theoretical formin distributions.

(H) Time courses of the length of protoplast aspirated into a micropipette (black) and the suction pressure applied by the pipette (blue). Measuring protoplast membrane tension required identifying the pressure ΔP at which the length of protoplast aspirated into the micropipette, l, is equal to the pipette radius R_p (see Fig. 2B). In this protoplast, $\Delta P \approx 175$ Pa.

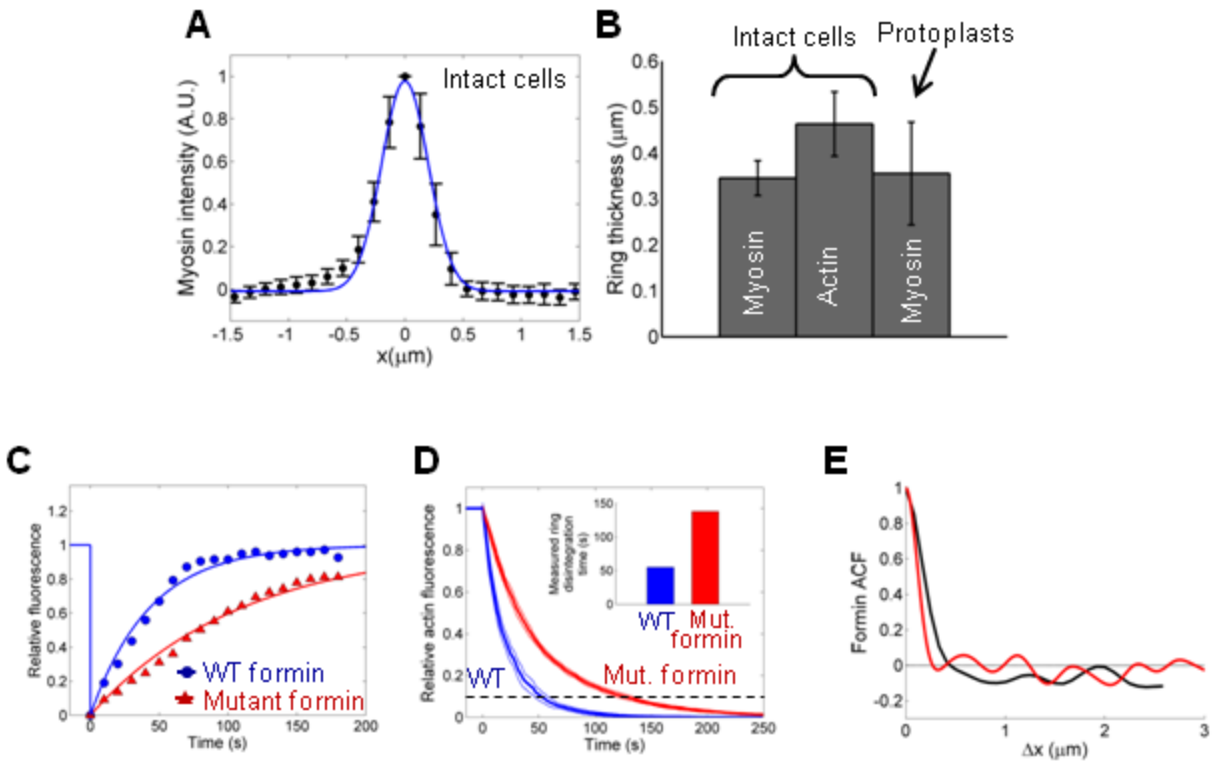
A
Intact cells
Myosin intensity (A.U.)
x(μm)
B
Intact cells
Protoplasts
Ring thickness (μm)
Myosin
Actin
Myosin
C
Relative fluorescence
WT formin
Mutant formin
Time (s)
D
Relative actin fluorescence
Measured ring disintegration time (s)
WT
Mut. formin
WT
Mut. formin
Time (s)
E
Formin ACF
Δx (μm)

Figure S3

Figure S3, related to Figure 3. Contractile ring thickness, testing the turnover mechanisms assumed in the simulation, and correlation function of formin in the ring.

(A-B) Measurement of ring thickness in the direction perpendicular to the plasma membrane from optical sections in the plane of contractile rings in protoplasts and intact cells (see Fig. 1J). To probe the ring thickness, intensity profiles were taken along lines parallel to the confocal planes to prevent artifacts from the reconstruction (yellow lines in Fig. 1J).

(A) Filled circles: mean of 20 linescans across the ring thickness in intact cells; error bars indicate SD. Blue curve: best-fit Gaussian.

(B) Comparison of the thicknesses of contractile rings in intact cells (n = 20 rings) and protoplasts (n = 12 rings) expressing Rlc1p-tdTomato to label myosin-II or GFP-CHD to label actin filaments (error bars indicate SD). Best-fit Gaussians of the type shown in (B) were deconvolved with a theoretical point spread function approximated by a Gaussian of standard deviation $\sigma_{PSF} = 0.21\lambda/NA$, where NA = 1.4 is the numerical aperture and λ = 510 nm (GFP) or 581 nm (tdTomato) is the emission peak. Ring thickness was defined to be twice the standard deviation of the deconvolved linescan.

(C and D) Determination of the ring simulation turnover parameters and testing of the turnover mechanisms assumed in the simulation. See Extended Experimental Procedures for details.

(C) Determination of the formin dissociation rate parameter in our simulations, k_{off}^{for}, by exponential fits to observations of fluorescence recovery after photobleaching (FRAP) of Cdc12p-GFP in the contractile ring (Yonetani et al., 2008). (Blue) Wild-type formin recovered in $t_{1/2}$ = 30 s, corresponding to a formin dissociation rate constant of $k_{off}^{for} = 0.023\ s^{-1}$. (Red) Mutant formin with deletions of profilin binding sites dissociated more slowly, $k_{off}^{for} = 0.009\ s^{-1}$.

(D) Estimation of the rate constants for actin polymerization and actin filament severing by simulations of the time course of contractile ring disassembly following treatment of dividing cells with a high concentration of Latrunculin A. Yonetani et al. (2008) fixed and stained cells with Alexa546-phalloidin to measure the time course of contractile ring disintegration after treatment with 100 μM Latrunculin A, finding that 10% of actin rings remained (dashed line) after ~55 s in wild-type cells, and ~138 s in cells expressing *cdc12ΔPBD*. The thick red and blue lines are the mean simulated time courses of 10 rings (thin lines: ±1 SD) for (blue) wild-type and (red) *cdc12ΔPBD* cells. We used the wild-type disintegration data (blue) to help fit for the values of the actin polymerization rate v_{pol} = 70 nm/s (26 subunits/s) and actin filament severing rate r_{sev} = 1.8 $\mu m^{-1}\ min^{-1}$ (see Extended Experimental Procedures). We fit simulations of formin mutants (red) to the observations using the experimentally determined mutant formin dissociation rate from (C), and then using the mutant formin polymerization rate as a fitting parameter (v_{pol} = 12 nm/s), keeping all other parameters the same as in wild-type cells. The low polymerization rate is consistent with the reduced polymerization activity of the mutant formin (Yonetani et al., 2008), supporting the turnover mechanisms assumed in our simulation.

(E) Mean spatial autocorrelation functions of the fluorescence intensity of Cdc12p-3YFP measured in rings in compressed protoplasts (black; n = 17 rings), and measured in simulated rings (red; n = 8 rings, each 10 μm long). The curve from the simulations was calculated from formin profiles in simulated rings after convoluting them with a theoretical point spread function, as described in (B). Both experimental and simulated autocorrelation functions decay rapidly to values not significantly different from zero, showing that formins are randomly distributed around the ring.

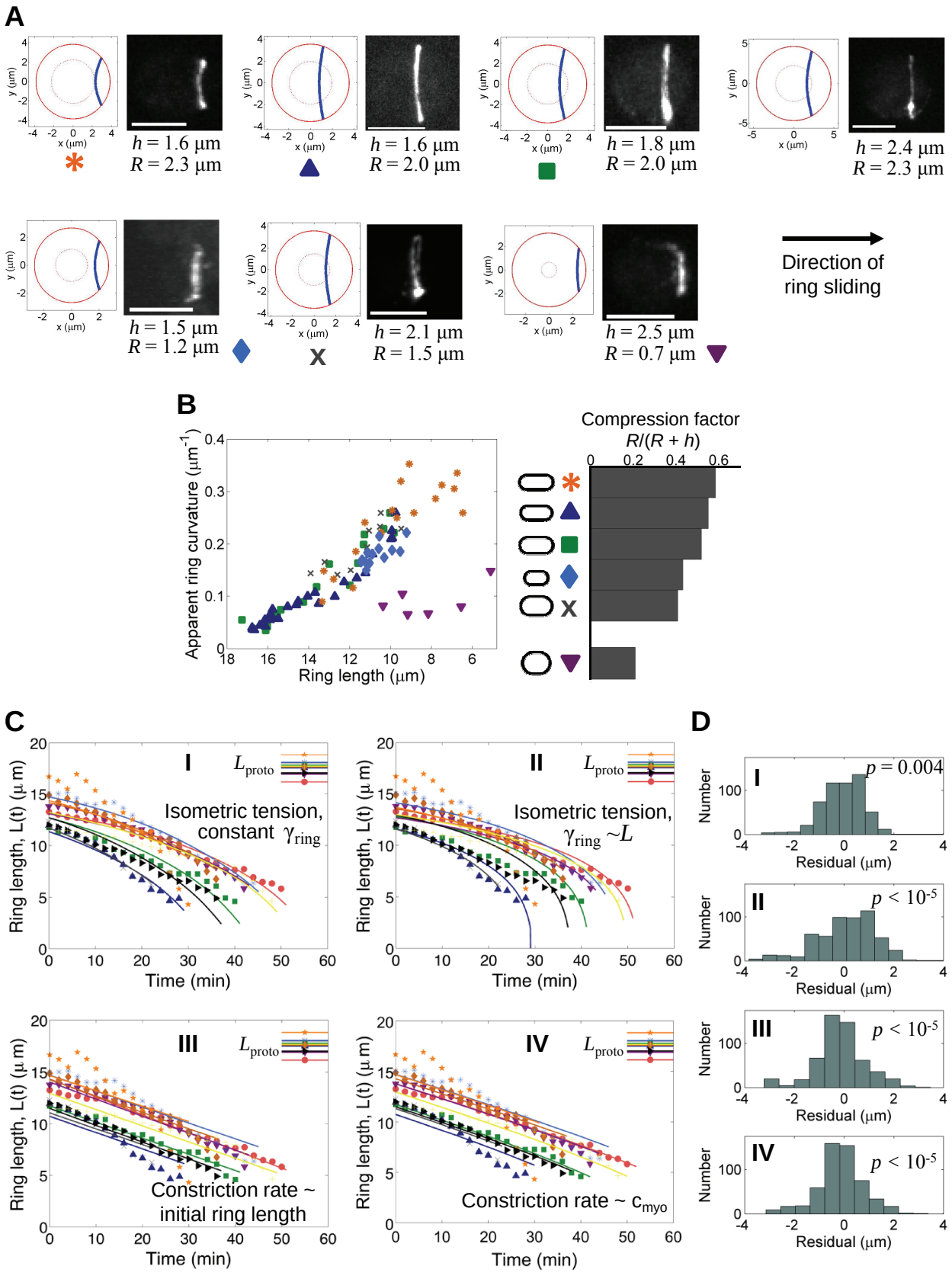
A
h = 1.6 μm
R = 2.3 μm
h = 1.6 μm
R = 2.0 μm
h = 1.8 μm
R = 2.0 μm
h = 2.4 μm
R = 2.3 μm
h = 1.5 μm
R = 1.2 μm
h = 2.1 μm
R = 1.5 μm
h = 2.5 μm
R = 0.7 μm
Direction of ring sliding
B
Apparent ring curvature (μm⁻¹)
Ring length (μm)
Compression factor
R/(R + h)
C
I
II
III
IV
L_proto
Isometric tension, constant γ_ring
Isometric tension, γ_ring ~L
Constriction rate ~ initial ring length
Constriction rate ~ c_myo
Ring length, L(t) (μm)
Time (min)
D
Number
Residual (μm)
p = 0.004
p < 10^-5

Figure S4

Figure S4, related to Figure 6. Comparison of observed and model-predicted ring shapes and length evolutions during ring constriction in fission yeast protoplasts.
(A) Comparison of ring shapes that were (Left) predicted by the sliding-constriction model with no free parameters from Eq. S20, or (Right) observed in maximum projections of confocal stacks of compressed protoplasts expressing Rlc1p-3GFP. Cells are arranged from highest to lowest degree of compression, with symbols corresponding to the key in panel B. In 6 out of 7 protoplasts the observed and predicted ring shapes were in close agreement (the exception was the cell at top right). Protoplasts are viewed from above. Solid red lines: cell boundary; dotted red lines: boundary of the flat portions of the cells. Bars: 5 μm.
(B) Measured ring curvature (as viewed from above) versus ring length for the 6 out of 7 protoplast contractile rings whose curvature we could measure. The key to the right shows cell shapes and compression factors. In agreement with model predictions, curvature increased over time as rings shortened (correlation coefficient $r = 0.84$, $n = 117$, $p < 10^{-30}$), and the least flattened protoplast had little curvature (purple triangles). Ring curvature was measured in ImageJ from the best-fit circle to a curve drawn over the ring as viewed from above.
(C) Least squares fits (solid lines) of four candidate models (numbered I-IV) to the experimentally observed time course of ring length during ring constriction for additional cells analyzed not shown in Fig. 6E (n = 10 additional cells included in the fit).
(I) Standard sliding constriction model in which the ring operates at isometric tension conditions with a tension at each length given by our ring simulation. We fit model predictions for $L(t)$ calculated from Eqs. S19 and S20 to all 17 measured curves simultaneously for a single value of the drag coefficient, after calculating ring tension as a function of ring length from our ring simulation using the measured myosin-II concentrations of the inset of Fig. S1H as input. This model best matched the experimental measurements
(II) The same model as (I), but with a drag coefficient proportional to ring length. This model generated constriction curves with larger curvature than observed.
(III and IV) Models where rings set their own constriction rate rather than setting their tension. Measurements from all cells were fit simultaneously for a single value of the ring shortening rate (III) per initial ring length or (IV) per relative myosin concentration.
(III) Rings had constant constriction rates proportional to initial ring length as in (Carvalho et al., 2009). This model failed to reproduce the observed curvature in the constriction profiles.
(IV) Ring constriction rates were proportional to the myosin concentration. This model failed to reproduce the observed curvature in the constriction profiles.
(D) Histograms of residuals for the four model fits shown in (C). Indicated p-values are from chi-squared tests for normality.